Experimental, theoretical, and numerical investigation of the homogenization of density nonuniformities in the periodic transport of a space-charge dominated beam

I. Haber

Plasma Physics Division, Naval Research Laboratory, Washington, D.C. 20375

D. Kehne and M. Reiser

Electrical Engineering Department and Laboratory for Plasma Research, University of Maryland, College Park, Maryland 20742

H. Rudd*

Berkeley Research Associates, Springfield, Virginia 22150

(Received 11 March 1991)

The homogenization of a beam with a transversely nonuniform initial density distribution is examined by masking the ouput from a Pierce electron gun into five parallel beamlets, which are then propagated down a channel of periodically spaced solenoid focusing magnets. Experimental measurements, theoretical predictions, and PIC simulations are in excellent agreement for averaged beam quantities such as rms emittance and envelope radius. In addition, the fine-structure characteristic of the nonlinear evolution of the beam, including the formation of downstream images, is reproduced in detail by the simulations.

I. INTRODUCTION

Several applications of charged-particle-beam technology, such as free-electron lasers, heavy-ion ignited inertial fusion, and neutral beam particle weapon systems, require beams with both high current and low emittance for their success. This need for low-emittance beams has driven the exploration of possible causes of emittance growth in high-current beams and the resulting limits on beam brightness. One such limiting mechanism is the conversion of space-charge potential energy into kinetic energy. This process is present whenever a low-emittance beam with a nonuniformity in current profile propagates in a linear focusing channel. As the transverse density inhomogeneity relaxes toward a final uniform state, which is characterized by a lower space-charge potential energy, the difference in potential energy is converted to kinetic energy (emittance), usually within a plasma period.

Measurements on a substantial number of high-current sources have reported [1] emittances that are significantly greater than the intrinsic emittance calculated using the cathode temperature as the source of transverse kinetic energy. Furthermore, the emittance growth that results from any initial nonuniformity becomes increasingly important as beam current is increased. This is because, as will be explained later, the emittance growth added by conversion of space-charge potential energy can scale linearly with the current I. This will eventually dominate the $I^{1/2}$ scaling [2] normally associated with the intrinsic emittance that results from the particle thermal velocities as they are born from a cathode with constant current density.

The process of converting space-charge potential energy to emittance during beam propagation in a linear-transport channel has been extensively investigated [3–6]. Theory and simulations agree well when examining the basic energy conversion itself, as well as the dy-

namics of this process for simple initial distributions. This paper extends previous investigations to include detailed comparison of theory, simulations, and experiment, including the inherently nonlinear dynamics that are characteristic of a strongly inhomogeneous initial state. We will show that while the energy conversion, which depends on beam-averaged quantities, generally occurs within a plasma period as previously reported [5], both simulation and experiment show that complicated evolution of the beam cross section persists for much longer times.

The initial nonuniform configuration studied here consists of five parallel beamlets formed by masking a high perveance electron beam. This configuration is motivated by applications, such as heavy-ion fusion, where a large beam current with low emittance is required but where acceleration of the entire beam in one focusing channel can be difficult. It then becomes important to merge several beams while minimizing the resulting emittance growth. However, it is not the purpose of this work to design a merging system, as has been done previously [7].

In a previous paper describing this work [8], preliminary results comparing experiment, theory, and simulation were presented that verified the theoretically predicted final emittance, as well as the characteristic merging distance of the beamlets. Also reported was the unexpected appearance of downstream images of the initial beam configuration. However, that work neglected to consider the adiabatic heating of the beam in the gun structure during compression from the cathode to beam waist. This led to the assumption of too small an initial emittance, which precluded good agreement between experiment and simulation of the downstream image formation. Some refinement of the model of the focusing magnets has also been necessary for good agreement.

In addition, this work presents more detailed compar-

isons of the experimental, theoretical, and simulated dynamics of the nonlinear evolution of the five-beamlet system. Emphasis is placed on the refined level of detailed agreement between simulation and experiment that was obtained by using the simulations to aid in determination of difficult-to-measure conditions, such as beam emittance at the gun output.

Three sections, describing theoretical expectations, the experimental configuration, and a description of the simulation model, are followed by a discussion of detailed comparisons between simulation and experiment and a final section of conclusion.

II. THEORY

A. Background

The emittance growth that occurs as an initially nonuniform beam profile relaxes to uniformity has been extensively investigated with theory and simulations [3–7]. Good agreement has generally been obtained between simulation and a simple theoretical model. This theory calculates the excess kinetic energy as the difference in space-charge potential energy between the initially nonuniform cross section and a final state assumed to be uniform. Some possible complications to this simple picture will be noted below, however, which can affect the calculation of the beam evolution.

The conversion between potential energy and rms emittance generally occurs in a distance $\lambda_p/4$, where $\lambda_p = 2\pi v/\omega_p$ is the distance traveled by the beam in a plasma period, and $\omega_p = (q^2 n/\epsilon \gamma^3 m)^{1/2}$ is the laboratory-frame plasma frequency, with $\gamma = (1-\beta^2)^{-1/2}$ the relativistic contraction factor, v the beam velocity, c the speed of light, $\beta = v/c$, m the particle rest mass, and q the charge of the particle.

This quarter wavelength of the plasma oscillation $\lambda_p/4$ is the distance required for a perturbation, which is initially established by displacing a charge from its equilibrium position, to interchange its initial potential energy with kinetic energy. Such an initial displacement, if it is in the parameter range that can be described by linear theory, will then interchange its energy back to potential energy. The fact that the actual beam system does not generally return to its initial state implies that the dynamical process is not well described by a simple linear displacement from equilibrium position, and the dynamics of any plasma oscillations are substantially nonlinear. Nevertheless, a sloshinglike motion in the beam density, of the sort which would be expected from the simple picture of an initial inhomogeneity launching a large-amplitude plasma wave, is still observed. This sloshing is also accompanied by oscillations in the rms emittance if the initial density is sufficiently nonuniform to cause substantial net rms emittance growth.

In addition to large-amplitude plasma oscillations, which can persist for several plasma periods, the beam particles also undergo the characteristic betatron oscillations of focused beam systems. As will be discussed below, the space-charge depressed betatron period can be somewhat longer than the plasma period. Phenomena

characterized by this time scale, such as the image formation discussed below, are therefore observed somewhat downstream of the homogenization distance.

Another source of complication can arise when the focusing force is spatially modulated, as in a periodic focusing lattice, rather than constant. In that case, the lattice frequency is introduced in addition to the plasma and betatron frequencies already discussed. It is then possible for the beam to become unstable [9]. In that case the simple process described here is not useful for predicting beam evolution. In the presence of lens nonlinearities it is also possible for individual particle orbits to become unstable, and the emittance will grow as a result. This process, however, has been found to generally occur on a much slower time scale than the equilibration discussed here [10]. It is also possible for energy to be transferred between the longitudinal and transverse directions [11]. For the experimental parameter range discussed here, however, the periodic nature of the transport channel does not introduce significant deviations from what is predicted by consideration of the simple conservation of transverse energy appropriate to a uniformly focused beam system.

A third possible source of complication, even when invoking the simple principle of conservation of energy, occurs when the initial emittance is low enough that the beam energetics is dominated by space charge. In this regime, if the initial deviation from equilibrium is sufficiently large, the rms radius of the beam will change slightly during the transition to equilibrium. Due to just a small change in beam radius, there is enough change in potential energy [12] that the rms emittance growth can differ substantially from what would be predicted assuming a constant rms beam radius. It is then important to accurately determine the actual value of the radius after beam homogenization, either from simulation or experiment, in order to correctly calculate beam energetics. This effect is even more pronounced when the initial beam is not perfectly matched, in the rms sense, to the focusing channel. There is then additional free energy associated with the mismatch that can cause further emittance growth. Application of the more general model [12], which includes the extra source of free energy arising from changes in the rms radius, to calculate the emittance growth in our experiment, however, yielded only very small (of order 1%) corrections to the simple theory discussed below.

An interesting, and unexpected, experimental observation, already discussed in our previous paper, is the appearance of a downstream image of the initial beam configuration on a fluorescent screen. Apparently, a sufficient number of particles described orbits that were near linear, so that the original transverse beam structure was imaged after a half-wavelength distance in the particle betatron oscillations. This occurs despite the substantial and irreversible growth in rms emittance that is normally associated with nonlinear behavior.

The appearance of images in the experimental beam system does, therefore, suggest that the linear-orbit approximation is germane to describing beam dynamics. As will be discussed below, the linear treatment can give

considerable insight into the nature of the detailed particle orbits. The details of the fine structure actually suggest that two sets of images, corresponding to different types of particle orbits, are observed in both the experiment and simulations. Furthermore, if a linearized treatment succeeds in appropriately describing the beam evolution for a beam with the large level of initial nonuniformity described here, it is likely to be even more appropriate for initial distributions that are somewhat more homogeneous.

B. Theoretical relationships

It has been known for some time that, in the presence of linear forces, the Kapchinskij-Vladimirskij (KV) envelope equations are also valid for a general distribution when the quantities in the original envelope equations represent the rms averages for the beam radius and emittance [13,14]. Such a beam suffers rms emittance growth only in the presence of nonlinearities in either the external or self-forces.

It is convenient to introduce a twice-rms or "effective" radius $R = 2R_{rms}$, and a similarly defined effective four-times rms emittance $\epsilon = 4\epsilon_{rms}$. These rms equivalent quantities are convenient when referring to a near-uniform distribution because the effective radius is equal to the actual radius for a uniform distribution.

Several authors [4,13,15] have generalized the rms envelope equations to include the consequences of emittance change due to nonlinearities in the beam system. A convenient formulation for the current case calculates the change in rms emittance, as an initial nonuniform cross section evolves to a final condition where it is assumed to be uniform, by using conservation of the sum of electrostatic potential and kinetic energy in the transverse direction [3,4]. The emittance growth can be written as

$$\frac{\epsilon_f}{\epsilon_i} = \left[1 + \frac{U}{2w_0} \left[\frac{\sigma_0^2}{\sigma^2} - 1 \right] \right]^{1/2} , \tag{1}$$

where $w_0 = \mu_0 I^2 / 16\pi\beta^2$, and U/w_0 is a dimensionless quantity that depends only on the shape of the initial nonuniform distribution, ϵ_f and ϵ_i are the final and initial four-times rms emittances as defined above, σ and σ_0 are, respectively, the phase advance per cell of the magnet period with and without self-fields, I denotes the beam current, and $\mu_0 = 4\pi \times 10^{-7}$ H/m is the permeability of free space.

If the phase advance per magnet period neglecting space charge σ_0 is less than 90°, the beam radius does not vary significantly during a period and the envelope characteristics can be accurately approximated by averaging the applied focusing force over the magnet period. In this smooth approximation [16] an effective matched radius R_m can be calculated for the periodic transport system by balancing the focusing force averaged over the period against the space-charge and emittance forces. The effective matched radius can be written as

$$R_m = (\epsilon_i S / \sigma_0)^{1/2} [u + (1 + u^2)^{1/2}]^{1/2} , \tag{2}$$

where S is the lens period, $u = KS/2\sigma_0\epsilon_i$, K is the generalized perveance defined as $K = (I/I_0)2/(\beta^3\gamma^3)$, and $I_0 = 4\pi\epsilon_0 mc^3/q \simeq 1.7 \times 10^4$ A for electrons, m and q are the electron charge and mass, c is the speed of light, and ϵ_0 is the permittivity of free space. In the experiment, the period length was $S = 13.6$ cm, and the measured current was 44 mA at 5 kV corresponding to a generalized perveance of $K = 1.88 \times 10^{-3}$. As discussed in our previous paper [8], a phase advance of $\sigma_0 = 70°$ was obtained by actually integrating the particle orbits through a period, using the nominal 83-G peak axial magnetic field and the analytic parametrization of the magnets discussed below. Note, however, that the nominal values for σ_0 and the peak magnetic field will be reexamined in Sec. V.

The smooth approximation can also be used to calculate the space-charge depression of the phase advance from the relationship

$$\frac{\sigma_0^2}{\sigma^2} = \frac{KR_m^2}{\epsilon^2} + 1 . \tag{3}$$

Equations (2) and (3) can be used to approximate the phase advance of individual particle trajectories, assuming their orbits are close to the linear orbits that would occur in a beam with a uniform cross section, such as what occurs in a K-V distribution. If the orbits are in fact close to linear, then an image of the initial inhomogeneous distribution would be expected to occur after traversal of a distance $z_{image} = \pi S / \sigma$ corresponding to a depressed phase advance of 180°.

It can be argued that two possible emittances are appropriate for use when calculating the depressed phase advance in order to estimate the image plane location. If the orbits of the particles forming the image remain local to the specific beamlet where they originate, the initial emittance of the beamlet seems correct. On the other hand, since the charge homogenization and the resulting growth in rms emittance occur after traversing a length that is short compared with the image formation distance, another estimate of the location of the image is obtained by using the value of effective emittance after homogenization. This estimate implies that orbits of the particles forming the image sample an average of the total beam. Both theoretically predicted distances can be compared with the experimentally observed and the simulated location of the image plane. As will be discussed below, there is some evidence of images at both planes.

From Eqs. (1) and (3) it is possible to rewrite the formula for emittance growth in terms of easily calculable quantities as

$$\frac{\epsilon_f}{\epsilon_i} = \left[1 + \frac{KR_m^2}{2\epsilon_i^2} \frac{U}{w_0} \right]^{1/2} . \tag{4}$$

If the current density from the cathode is assumed constant, the source current can be increased by making the cathode radius larger. If the gun geometry is also scaled to the larger radius, with any external focusing scaled to preserve this current density, then both K and R_m^2 are proportional to current. If the emittance growth due to

the conversion of space-charge potential to kinetic energy is further assumed to be the dominant source of emittance, then the emittance growth predicted by Eq. (4) is proportional to current. The intrinsic emittance that results from the cathode temperature, on the other hand, is proportional to the radius, and therefore to the square root of the current. This scaling, which can be shown in more generality than space here permits, is the source of the assertion that emittance growth from beam inhomogeneity can dominate the intrinsic emittance as current is increased by increasing the diameter of a cathode with constant current density.

In terms of the defined quantities, the charge homogenization distance $z_p = \lambda_p/4$ can be expressed as

$$z_p = \frac{\lambda_p}{4} = \frac{\pi\beta c}{2\omega_p} = \frac{\pi\overline{R}}{2(2K)^{1/2}} , \qquad (5)$$

where $\overline{R}$ represents the beam radius averaged over the merging distance. Because of the large excursions of the envelope during traversal of the matching sections, this is most accurately calculated from the actual beam envelope derived from the simulations.

Figure 1 is a schematic illustration of the experimental setup near the electron gun. The beam mask, as illustrated in the figure, is used to create an initial inhomogeneous current distribution consisting of five beamlets. The effective, or twice-rms, radius of the five-beamlet configuration at the mask is calculated to be

$$R_i = (a^2 + 1.6\delta^2)^{1/2} = 3.924a = 4.67 \text{ mm} . \qquad (6)$$

The intrinsic rms emittance of the five-beamlet configuration can then be calculated as the product of the initial effective radius at the mask and the beam thermal speed at that position. The thermal speed is in turn calculated using the measured cathode temperature corrected for the, assumed adiabatic, compression from the cathode to the beam waist, which is also the location of the mask. The effective, or four-times rms, emittance at the mask is therefore

$$\epsilon_i = R_i(2kT_w/eV_0)^{1/2} . \qquad (7)$$

where k is Boltzmann's constant, e is the electron charge, V_0 is the accelerating voltage, and T_w is the temperature at the beam waist (mask). Because the beam profile is not completely uniform as it emerges from the gun, calculation of ratio of the waist temperature to the cathode temperature, which is about a factor of 4, will be discussed below.

For the nonuniform field geometry factor U/w_0 one obtains

$$\frac{U}{w_0} = 0.16 \left\{ \ln \left[\left[\frac{\delta}{a} \right]^5 \left[\frac{1-s^8}{4} \right]^4 \right. \right.$$
$$\left. \left. \times \left[\frac{t^2 + 1.6s^2}{s^2} \right]^{12.5} \right] - 5 \right\} = 0.2656 , \qquad (8)$$

where $s = \delta/b$, $t = a/b$, and $b = 14$ mm is the pipe radius, as illustrated in Fig. 1.

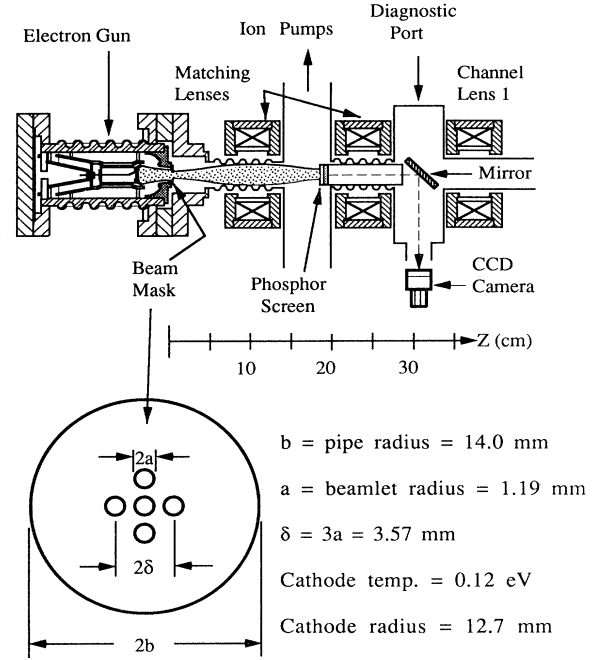Recent theoretical calculations have estimated the ex-

FIG. 1. Schematic of the multiple-beam experiment showing the first three magnets and the first diagnostic port. Also shown are the dimensions of the beam mask. A phosphor screen is mounted at the end of a trolley that can be moved along the channel.

cess space-charge potential energy that results from any mismatch in the beam envelope [12]. This energy is converted to emittance as the beam evolves. However, because the beam is well matched in the experiment, only about a 1% change in emittance is predicted from this effect, and these calculations are not presented here.

Using the expressions derived and the nominal experimental parameters, it is possible to predict the emittance growth that is expected in the experiment. This calculation, along with a discussion of the suitability of using the nominal parameter set, will be examined in Sec. V.

III. DESCRIPTION OF EXPERIMENT

The beam-transport apparatus used in the experiment [17] was designed to investigate the space-charge limited transport of low-emittance beams that are characterized by a sufficiently low spread in longitudinal velocity that all particle dynamics can be described nonrelativistically in a frame moving with the beam. Beam dynamics in this frame can then be described by a relatively small number of free parameters so that the experiment can be used, on a scaled basis, to investigate a range of phenomena relevant to a large number of low-emittance beam experiments. The scaled behavior of this experiment can be particularly useful for examining the nonlinear dynamics of ion beams because of the expense of any experimental apparatus that actually uses high-current low-emittance ion beams.

The basic experimental apparatus consists of a 2.54-

cm-diam thermionic cathode in a Pierce gun structure producing a 240-mA beam at an energy of 5 keV, and a measured cathode temperature $kT = 0.12$ eV. The intrinsic emittance, calculated by multiplying the thermal cathode velocity by the cathode radius, is low enough that the beam is space-charge dominated. That is, the beam envelope dynamics is determined primarily by space charge, rather than by the emittance due to beam temperature. The pulse length is 2 μs with a repetition rate of 60 Hz, so that diagnostics can be performed with relatively slow electronics, and the pulse-to-pulse repeatability allows reliable measurements over many pulses.

The beam compresses from the cathode to a waist that occurs at the exit from the anode. After passing through a mask placed at the plane of the waist, the beam then enters into a transport system consisting of 38 solenoidal magnets placed 13.6 cm apart. The first lens, centered 10.0 cm from the beam waist, and the second lens are independently powered, so that the values of their magnetic fields can be set to match the beam to the remaining periodic transport system.

The schematic diagram of the experimental apparatus in Fig. 1 shows the matching lenses and the first of the 36 periodic transport magnets. Also shown is the first diagnostic port. Additional diagnostic ports are available after 12, 24, and 36 lenses further down the channel.

A slit and pinhole apparatus [18] with a Faraday cup for measurement of the current, is used to measure the beam emittance and is mounted at the downstream end of the transport system. The measurement method used assumes cylindrical symmetry of the beam distribution. Because this apparatus cannot access the beam near the source when the magnetic transport system is in place, emittance measurements of the source have been performed using a special test stand constructed for that purpose.

Test-stand emittance measurement of the source, without the mask in place, obtained a value 1.1 times the intrinsic emittance calculated from the product of beam radius and the rms velocity derived from the measured 0.12-eV cathode temperature. Because use of rms quantities strongly weights particles at the outside of the beam, the emittance appropriate to the masked beam configuration in Fig. 1 is likely to be somewhat closer to that calculated from the intrinsic emittance. This is because the beam is observed to be somewhat hollowed, and the mask eliminates a large fraction of the higher-temperature particles at the beam edge, as will be discussed below.

The gun operating conditions between the solid and multibeam conditions are similar. This is evidenced by the 44-mA current that is measured coming through the beam mask, compared to the 46-mA current that is predicted by multiplying the 240-mA gun output by the ratio of the area of the beam waist to the combined area of the five beamlets.

A diagnostic tool that has proved central to the comparisons between experiment and simulation is a phosphor screen mounted on a trolley that can move down the entire channel to within 3 cm of the aperture plate.

The screen picture is recorded with a charge coupled device camera. The output is digitized on an Apple Macintosh computer, and the digital images are then displayed, measured, and recorded.

In order to accurately understand transport system behavior, especially in the relevant space-charge-dominated regime, it is important to have a thorough characterization of the transport system lenses. Extensive measurements have been made of the linear and nonlinear magnet characteristics and their analytic parametrization [19]. This will be discussed in later sections.

An extensive series of measurements has also been made of the propagation of the full, unmasked 240-mA beam in the periodic channel [20]. Good agreement has generally been obtained between simulations and measurements of the beam emittance at the downstream end of the experiment [21]. In particular, in those instances where substantial emittance growth was observed, simulations with the appropriate level of misalignments could account for the amount of emittance growth. Under conditions of misalignment, the beam density profile in the simulations evolves to a downstream density profile that is peaked on axis, and this general shape was verified experimentally. When the transport system was more accurately aligned, the somewhat-lower downstream emittance growth that was observed was also in good agreement with simulation. The simulations in this case predicted the 20% hollowing in beam density between axis and outer edge that is observed experimentally. This hollowing results from the formation of a space-charge distribution that is in equilibrium with the radially nonlinear focusing forces characteristic of the focusing magnets.

IV. NUMERICAL MODEL

If the electron beam in the Maryland transport experiment is viewed as a thermal, non-neutral plasma, then its transverse dimension is comparable to the Deybe length in that plasma. Additionally, the beam lifetime in traversing the transport system is only a few plasma periods, and the beam dynamics can be described nonrelativistically in the beam frame. This parameter range is particularly amenable to investigation using electrostatic plasma particle-in-cell (PIC) numerical techniques. The simulation of heavy-ion fusion transport (SHIFT) code [22] employed in the simulations here is a mature code based on well-tested plasma-simulation techniques [23]. This code should be capable of simulating the experiment to a high degree of accuracy if care is taken to adequately specify the correct experimental parameters.

The SHIFT code uses a fast-Fourier transform (FFT) field solver in conjunction with a capacitance matrix to solve for the image charges appropriate to arbitrarily shaped conducting boundaries. In the present case, the conductor geometry is a circular pipe.

A substantial number of numerical tests have been performed to identify the numerical parameters needed for accurate simulation. These simulations are generally performed on a 256 by 256 rectangular mesh, using 32 steps per magnet period and 32-K particles. The number of particles is determined more by a desire to smooth granu-

larity in rendering beam density plots than for any accuracy requirements in the simulations, and no differences in rms beam quantities are observed when fewer particles are used. Particles are advanced in time in a frame moving linearly with the beam, but not rotating, using the standard $\frac{1}{2}\mathbf{E}$, $\mathbf{v}\times\mathbf{B}$, $\frac{1}{2}\mathbf{E}$ centered leapfrog.

Many of the observed characteristics of the Maryland transport experiment may be explained only if the details of lens nonlinearities are included. It is therefore important to incorporate an accurate representation of the magnet characteristics into the simulation model. Fortunately for this purpose, a comprehensive series of detailed measurements of the lens characteristics has been made by Loschialpo [19]. He found that the longitudinal magnetic fields along the axis of a single lens could be accurately modeled by the analytic form

$$B_z(0,z) = \frac{B_0 e^{-(1/2)(z/b)^2}}{1 + \left[\dfrac{z}{a}\right]^2} \, , \tag{9}$$

where $b = 2.29$ cm and $a = 4.4$ cm. The off-axis magnetic field at a point (r,z) is then found numerically from the expansion up to fourth order,

$$B_z(r,z) = B_z(0,z) - \frac{r^2}{4}B''(0,z) + \frac{r^4}{64}B^{iv}(0,z) \, ,$$
$$B_r(r,z) = -\frac{r}{2}B'(0,z) + \frac{r^3}{16}B'''(0,z) \, . \tag{10}$$

Figure 2 is a plot of the measured values of the radial magnetic field 1.0 cm off axis, which is approximately the outer limit of the field typically sampled by beam particles. Also plotted for comparison is the field calculated from the truncated series. The value of B_0 used in the
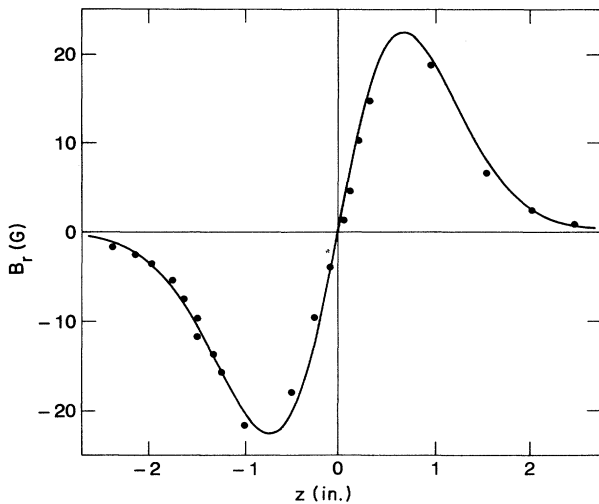

FIG. 2. Comparison, as a function of axial position, between the measured radial magnetic field at 1-cm radius and the field calculated from the truncated field expansion of the analytic expression for the on-axis field.

field calculation was in turn calculated from the applied magnet current using Loschialpo's measurements along the axis. There are no other free parameters in this comparison, except that the experimental data were symmetrized by slightly shifting the vertical axis to account for hysteresis in the field measurement.

During a simulation, the analytic expressions for the derivatives of the magnetic field are evaluated at each longitudinal position, and the magnetic field is then calculated using the radius of each particle. The need for 32 leapfrog steps per magnet period in integrating the particle orbits was determined numerically to be adequate for representing the relatively rapid variation in magnetic field near the beam edge.

V. COMPARISON OF EXPERIMENT TO THEORY AND SIMULATION

A. Use of images to determine experimental parameters

In addition to characterizing the experimental beam by measured macroscopic averages such as rms radius and rms emittance, and comparing the evolution of these quantities to theory and simulation, a more detailed level of comparison is made possible by the fluorescent screen diagnostic. A wealth of information is contained in the fine structure observed during beam relaxation to a uniform cross section, and simulation should be capable of reproducing this fine structure at every location along the transport system. Furthermore, it is unlikely, because of the observed complexity of the beam evolution, that good agreement can be obtained between simulation and experiment unless the simulation code is a very good representation of the experimental apparatus.

Because of the unexpected observation on the fluorescent screen of a downstream image of the initial five-beamlet distribution, emphasis was placed on using the simulations to duplicate the location, detailed shape, and orientation of the beam images, as well as details of the beam evolution leading to the image formation. It was hoped, and to some degree this was ultimately verified, that if a simulation could reproduce the beam images, it would also reproduce the intermediate dynamics of their formation.

Simulations that employed the nominal experimental parameters, however, did not adequately reproduce details of the observed images. A search of parameter space was therefore undertaken to identify which parameters, when varied from the nominal values, would account for the observed discrepancy between observed and simulated profile evolution. This parameter search first emphasized variation in those parameters most subject to experimental uncertainty, such as initial beam emittance, beam waist location, and initial beam distribution. This procedure led to the discovery that, in the simulations described previously [8], the value of the beam temperature at the mask did not include the adiabatic heating of the beam during compression from the cathode to anode.

The "best fit" between simulation and experiment did reproduce a beam image at almost the correct location. However, this required use of an initial emittance in the

simulation approximately 25% higher than the intrinsic emittance calculated from the mask configuration and the temperature at the mask plane after adiabatic compression from the cathode. In view of measured solid beam emittances on the test stand within 10% of the intrinsic emittance, and the likelihood that rejection of the high-temperature edge particles by the beam mask should result in an emittance closer to the intrinsic value in the five-beamlet experiment, this seemed too high. Furthermore, the simulated image shapes were somewhat different than those experimentally observed, and the values of the matching lens currents needed to simulate a matched beam were outside of the range of measurement uncertainty. Finally, at the image plane 101 cm from the mask, the observed images were rotated approximately 360° from their initial orientation. This did not correspond to the 328° rotation predicted both by simulation and by simple paraxial theory using the analytic field in Eq. (9).

Because of the experimental observation that some stray magnetic field could be present at the cathode when the beam pulse did not correspond to the minimum in the 60-Hz heater current, and in view of the possible observed discrepancy in beam rotation, care was exercised to insure that experimental observations were always performed at a null in the 60-Hz cycle. As a further check, simulations were performed to investigate the conse-

quences of an added magnetic field at the source. Only when this field is set to approximately 10 G, which is the maximum possible in the experiment, was any substantial effect observed on the formation of images, and the images then seen were somewhat different in form from what was actually observed.

It was accordingly decided to relax previous assumptions as to which parameters were inviolable in searching for agreement, and a systematic, if tedious, attempt was made to widen the simulation parameter range examined in seeking a best fit to the experimental observations. Fortunately, the rotation that a beam experiences in traversing a periodic solenoidal transport system depends strongly only on the values of the magnetic field. In particular, when the magnetic field is scaled upward by 10%, keeping constant the functional form for the spatial variation in the magnetic fields, the rotation of the simulated beam agrees well with the observed rotation.

Figure 3 is a comparison between the fluorescent screen images and grey-scale computer renderings at various positions along the transport system when the 10% above nominal magnetic field is used. The initial emittance used in this simulation is approximately 65 mm mrad; however, variations of about 5% from this value do not substantially change the location and shape of the simulated images. The computer renderings were generated by binning the particle data from the simula-

EXPERIMENT   SIMULATION   EXPERIMENT   SIMULATION

z = 3.4 cm   z = 44.3 cm

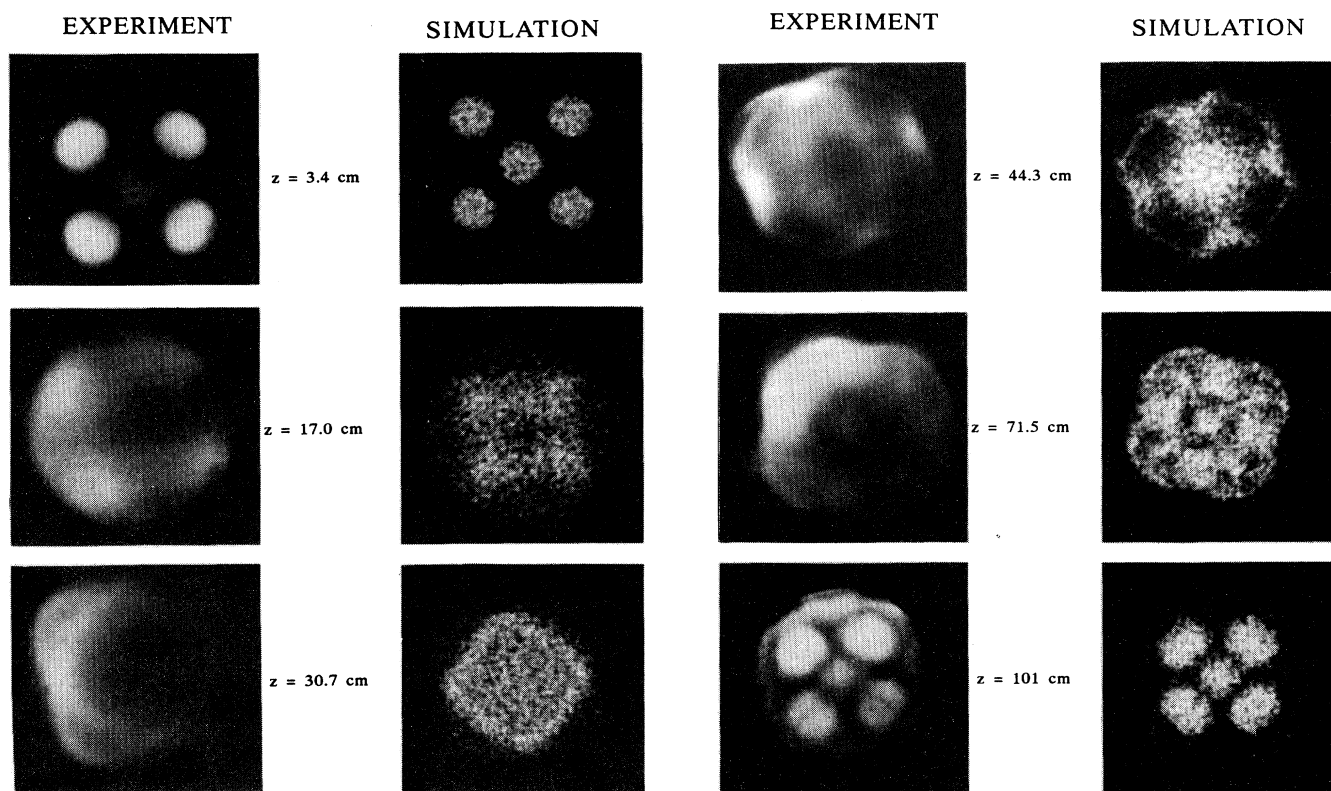z = 17.0 cm   z = 71.5 cm

z = 30.7 cm   z = 101 cm

FIG. 3. (a) Phosphor-screen pictures and comparable simulation plots at 3.4, 17.0, and 30.7 cm from the beam mask, showing beam profile evolution and image formation as the beam propagates down the periodically focused channel. (b) Phosphor-screen pictures and simulation plots at 44.3, 71.5, and 101.0 cm.

tion, attributing a grey scale to each level, and then plotting the corresponding bin in the appropriate grey. It should be noted that the mask orientation in the experiment, as can be noted in the first of the fluorescent screen images, is rotated by approximately 7°. The orientation of the simulated images was therefore adjusted to match the experimental pictures tilted by this 7°.

Excellent agreement is evident not only in the location and shape of the images but also in many fine details of the structure. Though not shown, both simulation and experiment also show some circularly symmetric beam structure 202 cm down the transport line, which is where a second image might be expected. Some deviations from azimuthal symmetry are observed in the experimental pictures that are not observed in the simulations. This is presumably due to a misalignment in the experimental apparatus that is not in the simulation.

Some discrepancy between the experimental and simulated images can be seen at $z = 3.4$ and 17.0 cm. Upon further examination, it was discovered that the structure of the beam at 3.4 cm in the experiment agrees quite well with the simulated beam at 6.4 cm. In addition, the structure seen in the experiment at 17.0 cm was found to agree with the simulated beam at 20.4 cm. This 3-cm difference appears consistently throughout the matching section ($z < 30$ cm). Past the matching section, agreement improves substantially.

In the channel experiment, when the beam is injected into the first matching lens it undergoes free expansion for the first 5–6 cm before being influenced by the first magnet located 10 cm from the mask. Therefore, the free expansion data measured on the test stand should duplicate the expansion found in the first 5–6 cm of the channel experiment. As it turns out, in the region 3–6 cm from the mask, the test-stand expansion of the five beams agrees very well with the simulation results and disagrees with the previous measurements of the five beams performed in the channel. After consideration of the mechanics of the phosphor screen trolley in the matching section, it was concluded that the observed discrepancy probably did result from an error in the positional measurement of the trolley in the matching section.

B. Comparisons of averaged beam parameters

A further consequence of employing a peak magnetic field 10% above the nominal value is resolution of the discrepancy between matching lens values measured experimentally and those needed to match the simulated beam. Figure 4 is a plot of the rms beam radius as a function of the distance along the transport line. The simulated beam envelope is now well matched for transport lens values at the $+10\%$ level, and the ratio of matching lens fields to transport lens fields set to the values found to match the beam in the experiment.

Though the setting of the peak value of the magnetic field primarily affects the beam rotation, the phase advance, and therefore the location of the beam images, is also shifted. In view of the difficulty in measuring the emittance at the mask plane, the emittance appropriate for the simulations was found by numerical experimenta-
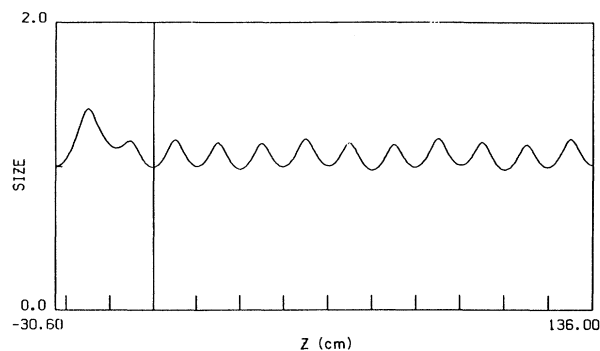

FIG. 4. Plot of the rms radius, normalized to the initial rms radius, of the simulated beam as it propagates down the channel.

tion. Using the augmented magnetic field necessary to get the proper beam rotation, the initial emittance was varied until the simulated images occurred at the location observed in the experiment. It is worth noting that this procedure appears to be a sensitive method for measuring beam emittance, since variations of the order of 10% result in a clearly observable shift of the images off their nominal location.

Table I is a summary of the beam parameters found experimentally, theoretically, and in the simulations. The initial value of emittance found by using the simulations to reproduce the image location is 64.8 mm mrad. This corresponds to a temperature at the mask that assumes adiabatic heating during a factor of 2.0 compression in beam radius going from the cathode to the mask. This compares with a factor 2.1, which is inferred by measuring the radius of the edge of the beam. However, as will be discussed below, because the solid beam is not homogeneous, an alternate compression factor can be calculated from the ratio of masked current to total current. The compression ratio calculated in this way, by dividing the ratio of compressed current to total cathode current by the ratio of cathode area to the total area of the holes in the mask, is 2.05. Both of these numbers verify, within the uncertainties, that the emittance at the beam mask is close to the intrinsic emittance. That is, the cathode temperature is the full source of the transverse thermal energy.

Figure 5 is a plot of rms emittance as the simulated beam propagates down the transport system. Little further change is observed in the remaining 26 periods. The final emittance grows by a factor of 1.54 to 100 mm mrad which agrees, within the combined measurement uncertainties, to the growth by a factor of 1.64 (108 ± 6 mm mrad) measured at the downstream end of the transport system by the slit pinhole method referenced above. Recalling that there is some uncertainty as to what initial emittance to use in the simulation, closer agreement could have been obtained to the measured final emittance by running the simulation with a slightly higher initial emittance, as might result from a small degradation of the beam from the intrinsic value.

From the theory of energy conservation as discussed in

TABLE I. Summary of results from experiment, simulation, and theory. The first three rows are input parameters for simulation and theory.

	Experiment	Simulation	Theory
Initial emittance ϵ_i (mm mrad)	66 ± 3[a]	64.8	64.8
Peak magnetic field B_0 (G)[b]	91.5 ± 2	91.5	91.5
Phase advance without space charge σ_0[c]	77°	77°	77°
Downstream emittance ϵ_f (mm mrad)	108 ± 6	100	98
Homogenization distance z_p (cm)	15–20	15–20	15
Image location z_{image}	101	101	103

[a]Determined from measured ratio of five-beam and full beam currents and assuming adiabatic compression for calculation of the mask temperature.
[b]Determined from measurement of image rotation.
[c]Determined by integrating over orbits using analytic B field with $B_0 = 91.5$ G.

Sec. II, growth by a factor of 1.58 to a value of 102 mm mrad is predicted if the nominal magnet field is assumed. If this calculation is redone for the assumed higher magnet field, and the corresponding value for σ_0 of 77°, the initial effective matched radius becomes $R_m = 4.61$ mm, and growth by a factor of 1.51 to a value of 98 mm mrad is predicted. In view of the uncertainties in accurately specifying the initial distribution function, as will be discussed below, as well as possible small residual misalignments in the transport system, agreement amongst theory, simulation and experiment is within the combined uncertainties.

The appearance of downstream images suggests that many particle orbits are well approximated by the trajectories that would be expected from linear orbits in a beam with a uniform transverse distribution. This assumption can be used to calculate the location of the image plane. Some further assumption is required about the average background distribution the particles traverse during their orbits. Alternatively, by using Eq. (3) to calculate the depressed phase advance, and by assuming that the

FIG. 5. Plot of the rms emittance, normalized to the initial emittance, of the simulated beam as it propagates down the channel.

images are indeed formed after a phase shift of π in the linear depressed phase advance, the location of the image plane can be used to infer the average effective background emittance sampled by the particles forming the image.

Using the smooth approximation, and employing the value of the magnetic fields from the simulations (that is nominal plus 10%) the phase advanced per magnet period σ_0 is 77°. If the initial beam emittance inferred from the cathode temperature is used, an image plane location of 103 cm is calculated, which compares well with the observed image plane location. This strongly suggests that the individual particles forming the image experience a background distribution largely composed of the unaltered initial beamlets, and suggests that the particle orbits are fairly localized in their excursions from initial positions. This would explain why the location of the image plane in the simulations is a sensitive function of the assumed initial emittance.

Because the rms emittance reaches its final value in a distance short compared with the image formation distance, it would have been expected that the emittance to be used in calculating the image plane location should be the value after homogenization. This assumption predicts an image plane location of approximately 69 cm. Examination of the simulation and experimental pictures at 71.5 cm does show evidence of an image being formed at this plane, although somewhat different in detail from the images further downstream. Though these images are less clear than the images further downstream, more distinct images are in fact seen in both the simulation and experimental pictures, not shown here, slightly further down the transport line. It is probably reasonable that formation of this set of images is slightly delayed since it takes the beam a finite time to reach the final emittance.

It can be conjectured from this behavior that the evolution of the beam cross section can be thought of as consisting of groups of particles whose orbits sample different parts of the beam as they traverse the transport
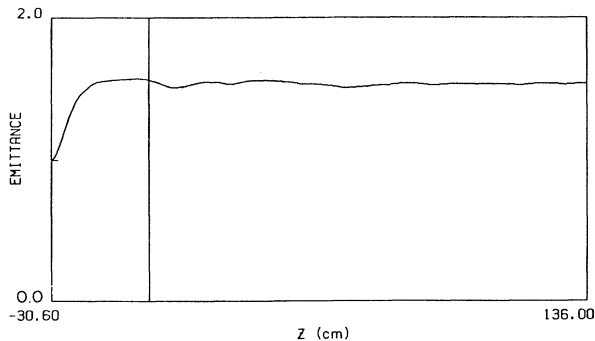
system. One of these groups samples mostly particles local to an initial beamlet, and therefore forms an image influenced by particles in the initial beamlet emittance. Another group samples a more global section of the beam and therefore images at a distance predicted by the average beam emittance, which grows rapidly as the beam homogenizes.

C. Reexamination of the magnet model

Particularly in view of the large number of detailed measurements that have been conducted to specify the magnets in the Maryland transport experiment, the need to assume a 10% increase in nominal field in order to get a good fit to the experimental data was surprising. To determine possible causes for this 10% discrepancy, a series of simulations was performed that attempted to match the previously published [19] magnet measurements. Additional measurements of magnet characteristics were also undertaken.

When the focal length of the magnet for a low-current beam was measured by running a low-current beam in the simulation code, the code agreed with the reported [19] experimental and calculated value to within the 1% measurement accuracy. The published data also include plots of the magnet characteristics for the full beam current, and these curves do not exhibit the excellent agreement that was achieved in similar comparisons of the low-current trajectories. Simulations were therefore run to compare directly to the published curves. The rms beam characteristics found in these simulations did agree very well with the published theoretical curves. However, for the case that had envelope excursions closest to what is relevant to the five-beamlet case, a much better fit to the experimental beam-edge data was, in fact, obtained by increasing the nominal field by 10%. Since both the analytic model and the parameter fit to that model were optimized for a beam with low current, it is possible that the analytic fit used is not as good for space-charge dominated flow, where particle orbits are nearly parallel to the axis.

Another possible source of discrepancy may reside in possible differences among the actual magnets. Recent measurements have, in fact, suggested that there are differences of a few percent between individual magnets. It is not, however, currently practical to disassemble the transport line and measure all the magnet characteristics in order to definitively resolve this issue.

D. Beam hollowing at the mask plane

Another area lacking clear agreement between simulation and measurement results from the observation that the beam entering the mask plane is somewhat hollow. An examination of the Fig. 3 fluorescent screen output at 3.4 cm shows less light output in the central beamlet. Figure 6 is a plot of the light output from a scan across the masked beam fluorescent screen output. The data, taken on the test stand, are from a plane within 1 cm of
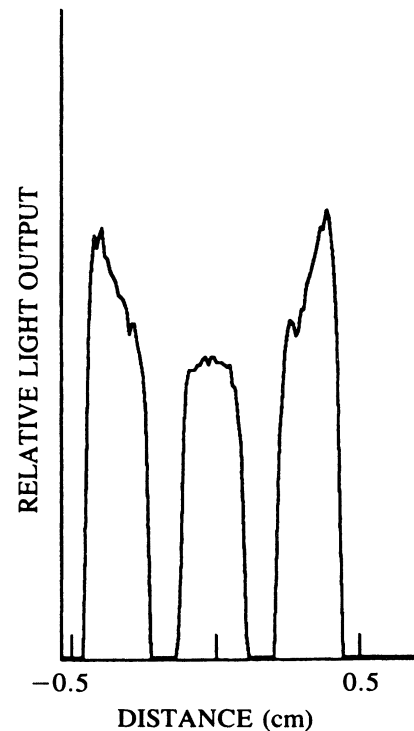

FIG. 6. Scan of the light output from the fluorescent screen across the beam just after it emerges from the mask. Hollowing of the beam profile is clearly visible.

the mask. This shows clear evidence of hollowing in the solid beam out of which the five beamlets were carved. The relationship between light output and current density was established using the Faraday cup and pinhole apparatus to calibrate a screen picture for the solid beam. From this calibration a ratio of about 1.25 between the current density at the beam edge and the beam center is inferred.

If phase-space area, or emittance, is conserved, the thermal velocity varies as the inverse of radius as the beam is focused down when going from the cathode to the gun waist. Because of the short distance between the cathode and the beam waist, this assumption of adiabatic heating of the beam seems to be a good approximation. In particular, it seems reasonable to further assume that the particle orbits in going from cathode to waist are relatively laminar, and this adiabatic temperature increase also occurs locally within the beam. This assumption of local adiabatic heating predicts an increased temperature at the beam edge corresponding to the increased density observed, and this increase has been verified by direct measurement using the slit and pinhole apparatus.

Simulations, on the other hand, that assume an initially hollowed current distribution, do not reproduce the experimental pictures as well as the simulations, presented thus far, which assume an initially uniform beam cross section. A typical simulation picture at the 101-cm image plane, generated with an initial ratio of 1.2 between the central and edge densities, is shown in Fig. 7. The tear-shaped images appear to be characteristic of simula-
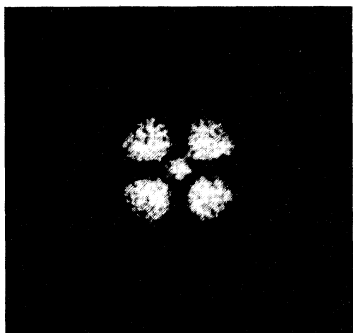
FIG. 7. Image plane profile, 101.0 cm from the beam mask, from a simulation using a beam that is initially hollowed by 20%. Tear-shaped images are typical of those seen in simulations with initially hollowed profiles.

tions that assume an initially hollowed beam. This discrepancy is not improved by assuming an initial temperature variation consistent with the concept of local adiabatic heating. Simple assumptions that were tried, such as a quadratic or stair-step approximations for the shape of the initial density and temperature, have not been successful at improving agreement. Variation of the other parameters such as current and emittance also do not circularize the teardrop shape of the beamlets in the image.

Unfortunately, the uncertainty in specifying the detailed magnet characteristics under the actual experimental conditions also complicates resolution of this other discrepancy. Because both the effect of nonuniform initial density and uncertainty in the radial dependence of the focusing strength, which depends on the magnet parametrization, are strongly interrelated in their effect on image shape, it is difficult to determine which effect is responsible for differences between simulated and observed

experimental behavior, especially in view of the narrow parametric range of the currently available experimental data.

VI. CONCLUSIONS

The nonlinear relaxation of an initially nonuniform beam cross section toward a uniform final state has been studied using experiment, theory, and simulation in concert. Good agreement to the theory presented has been demonstrated on the evolution of macroscopic averages such as the rms emittance. In addition, detailed comparison between fluorescent screen measurements and computer-generated grey-scale renderings of simulation output has been found to be a very valuable diagnostic technique, because a good match between the two sets of pictures can be obtained only after several free parameters have been adjusted.

The ability of the simulations to accurately reproduce many of the experimentally observed features of such a nonlinear beam system is a good benchmark of the capabilities of the numerical method. Also demonstrated is the usefulness of the numerical simulations as an aid in examining the consistency of differing sets of experimental measurements, as well as a tool for inferring quantities whose direct measurement can be quite difficult. In particular, the observed sensitivity of the evolution of the beam profile to the initial value of beam emittance suggests that measurement of this beam profile evolution, using a fluorescent screen or Cerenkov foil, and simulations in parallel with those measurements can be a useful method for inferring beam emittance.

ACKNOWLEDGMENTS

*Present address: Computer Sciences Corporation, Systems Science Division, Lanham, MD 20706.

[1] Charles W. Roberson, IEEE J. Quantum Electron. QE-21, 860 (1985).

[2] J. D. Lawson, The Physics of Charged Particle Beams (Oxford University Press, New York, 1988).

[3] J. Struckmeier, J. Kalbunde, and M. Reiser, Part. Accel. 15, 47 (1984).

[4] T. P. Wangler, K. R. Crandall, R. S. Mills, and M. Reiser, IEEE Trans. Nucl. Sci. NS-32, 2196 (1985).

[5] O. A. Anderson, Part. Accel. 21, 197 (1987).

[6] Ingo Hofmann and Jurgen Struckmeier, Part. Accel. 21, 69 (1987).

[7] C. M. Celata, A. Faltens, David L. Judd, L. Smith, and M. G. Tiefenback, in Proceedings of the 1987 Particle Accelerator Conference, Washington, D.C., 1987, edited by E. R. Lindstrom and L. S. Taylor (IEEE, New York, 1987), p. 1167.

[8] M. Reiser, C. R. Chang, D. Kehne, K. Low. T.Shea, H. Rudd, and I. Haber, Phys. Rev. Lett. 61, 2933 (1988).

[9] I. Hofmann, L. J. Laslett, L. Smith, and I. Haber, Part.

Accel. 13, 145 (1983).

[10] I. Haber and H. Rudd, Nucl. Instrum. Methods Phys. Res. A 278, 174 (1989).

[11] I. Hofmann, Nucl. Instrum. Methods 187, 281 (1981).

[12] Martin Reiser, J. Appl. Phys. (to be published).

[13] P. M. Lapostolle, IEEE Trans. Nucl. Sci. NS-18, 1101 (1971).

[14] Frank J. Sacherer, IEEE Trans. Nucl. Sci. NS-18, 1105 (1971).

[15] E. P. Lee, S. S. Yu, and W. A. Barletta, Nucl. Fusion 21, 961 (1981).

[16] M. Reiser, Part. Accel. 8, 167 (1978).

[17] J. McAdoo, E. Chojnacki, P. Loschialpo, K. Low, M. Reiser, and J. D. Lawson, IEEE Trans. Nucl. Sci. 32, 2632 (1985).

[18] M. J. Rhee and R. F. Schneider, Part. Accel. 20, 133 (1986).

[19] P. Loschialpo, W. Namkung, M. Reiser, and J. D. Lawson, J. Appl. Phys. 57, 10 (1985).

[20] D. Kehne, K. Low, M. Reiser, T. Shea, C. R. Chang, and Y. Chen, Nucl. Instrum. Methods A 278, 194 (1989).

[21] H. Rudd, I. Haber, C. R. Chang, D. Kehne, K. Low, M. Reiser, and T. Shea, Nucl. Instrum. Methods A **278**, 198 (1989).

[22] I. Haber, in *High-Current High-Brightness and High-Duty Factor Ion Injectors (La Jolla Institute in San Diego, California)*, Proceedings of the Workshop on High-Current, High-Brightness and High-Duty Factor Ion Injectors,

edited by George H. Gillespie, Yu-Yun Kuo, Denis Keefe, and Thomas P. Wangler, AIP Conf. Proc. No. 139 (AIP, New York, 1985) p. 107.

[23] Charles K. Birdsall and A. Bruce Langdon, *Plasma Physics via Computer Simulation* (McGraw-Hill, New York, 1985).
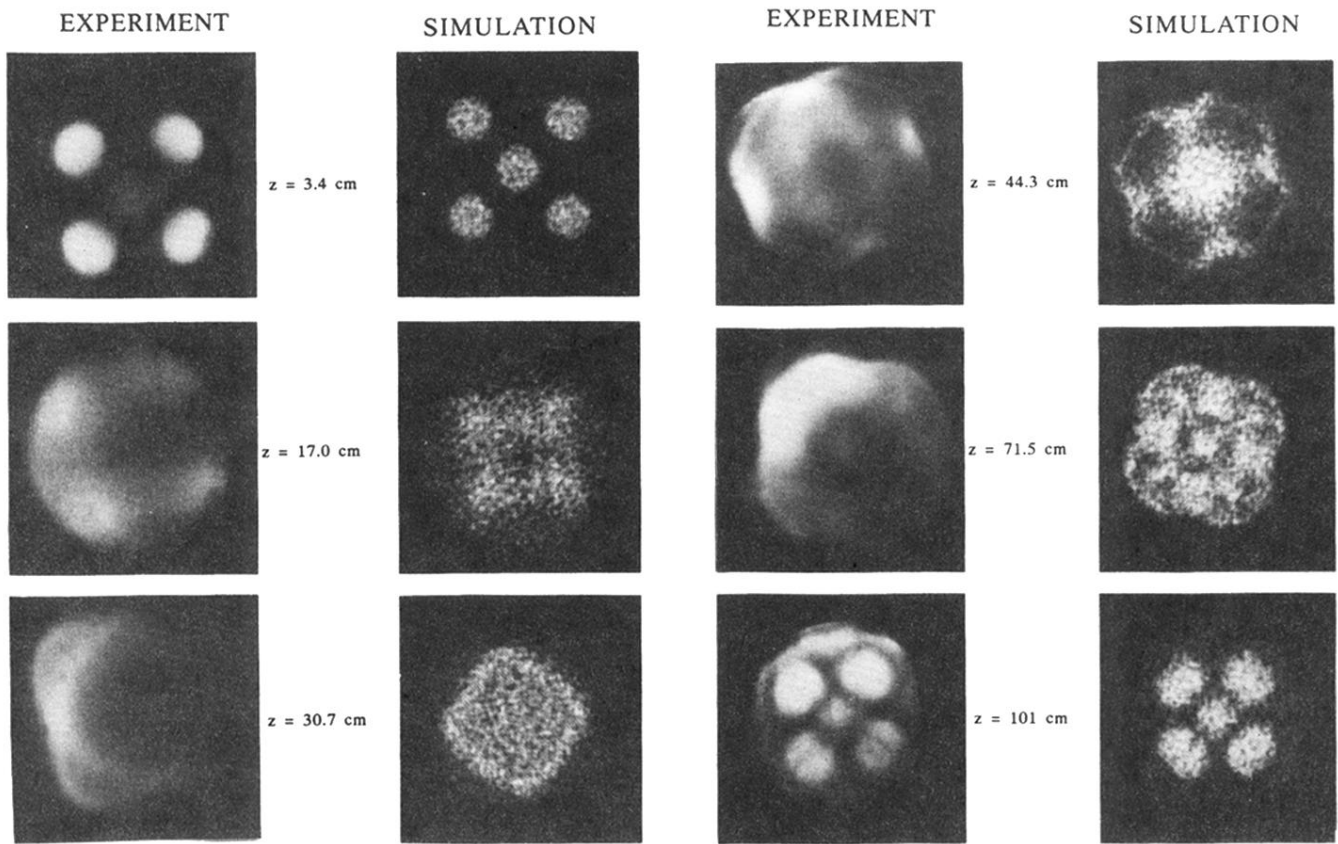
FIG. 3. (a) Phosphor-screen pictures and comparable simulation plots at 3.4, 17.0, and 30.7 cm from the beam mask, showing beam profile evolution and image formation as the beam propagates down the periodically focused channel. (b) Phosphor-screen pictures and simulation plots at 44.3, 71.5, and 101.0 cm.
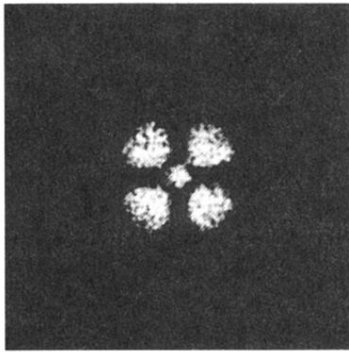
FIG. 7. Image plane profile, 101.0 cm from the beam mask, from a simulation using a beam that is initially hollowed by 20%. Tear-shaped images are typical of those seen in simulations with initially hollowed profiles.